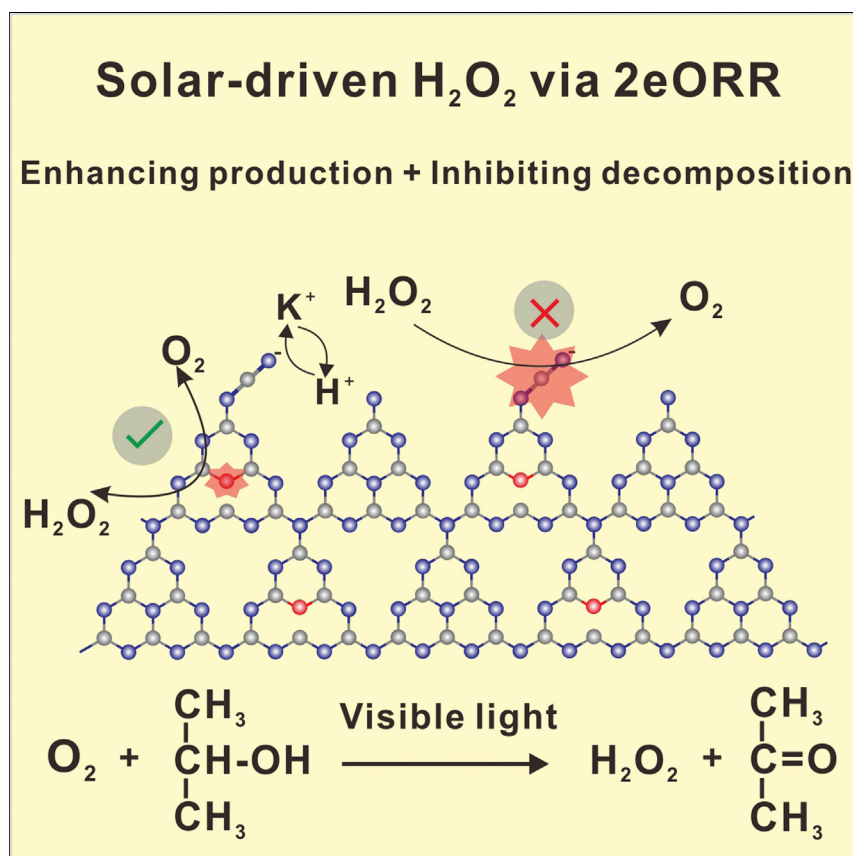


## Article

Rational design of carbon nitride for remarkable photocatalytic H<sub>2</sub>O<sub>2</sub> production

Zhao et al. demonstrate an example of photocatalyst design from theoretical guidance. Solar-driven H<sub>2</sub>O<sub>2</sub> production is improved by enhancing production efficiency and inhibiting the decomposition, providing commercial feasibility for the industrial production of H<sub>2</sub>O<sub>2</sub>.

Heng Zhao, Qiu Jin, Mohd Adnan Khan, Steve Larter, Samira Siahrostami, Md Golam Kibria, Jinguang Hu

samira.siahrostami@ucalgary.ca (S.S.)  
md.kibria@ucalgary.ca (M.G.K.)  
jinguang.hu@ucalgary.ca (J.H.)

**Highlights**

Carbon nitride-based photocatalysts were screened by DFT

Dual functions of producing and inhibiting H<sub>2</sub>O<sub>2</sub> were precisely synthesized

Heteroatomic oxygen and cyano group endowed photocatalyst for excellent H<sub>2</sub>O<sub>2</sub> generation

TEA provided the possibility and guidance of solar-driven H<sub>2</sub>O<sub>2</sub> commercialization



## Article

# Rational design of carbon nitride for remarkable photocatalytic H<sub>2</sub>O<sub>2</sub> production

Heng Zhao,<sup>1,4</sup> Qiu Jin,<sup>2,4</sup> Mohd Adnan Khan,<sup>1</sup> Steve Larter,<sup>3</sup> Samira Siahrostami,<sup>2,\*</sup> Md Golam Kibria,<sup>1,\*</sup> and Jinguang Hu<sup>1,5,\*</sup>

### SUMMARY

Photocatalytic oxygen reduction reaction (ORR) on graphitic carbon nitride offers a sustainable route to produce H<sub>2</sub>O<sub>2</sub>. However, the current solar-to-H<sub>2</sub>O<sub>2</sub> conversion efficiency is still limited by the high overpotential of 2e<sup>-</sup>-ORR process and *in situ* H<sub>2</sub>O<sub>2</sub> decomposition. Here, we aim to overcome these challenges by introducing the heteroatomic oxygen and cyano group. Density functional theory (DFT) study reveals that oxygen doping at the pristine position of graphitic nitrogen significantly contributes to reducing the overpotential for H<sub>2</sub>O<sub>2</sub> formation. The introduced cyano group coupled with amino nitrogen at the edge of crystalline nanosheets synergistically interacts with doped oxygen to further boost H<sub>2</sub>O<sub>2</sub> production and also efficiently inhibits H<sub>2</sub>O<sub>2</sub> decomposition. As a result, visible light-driven H<sub>2</sub>O<sub>2</sub> production at 5.57 mM/h is achieved along with selective counterpart oxidation of isopropanol to acetone at 100% selectivity. A rigorous process model combined with a techno-economic analysis (TEA) provides guidance for the development of an economically feasible photocatalytic H<sub>2</sub>O<sub>2</sub> production process.

### INTRODUCTION

Hydrogen peroxide (H<sub>2</sub>O<sub>2</sub>), being one of the top 100 important chemicals in the world, holds huge market potential in industry for wastewater treatment, disinfection, and pulp bleaching.<sup>1–3</sup> Currently, over 95% of the total H<sub>2</sub>O<sub>2</sub> is produced in industry by the anthraquinone oxidation process, which suffers from high energy consumption and toxic emissions.<sup>4</sup> Alternatively, solar-driven water oxidation or oxygen reduction in the presence of saturated oxygen or air provides a promising route to produce H<sub>2</sub>O<sub>2</sub> under mild, safe, and low carbon intensity conditions.<sup>5–8</sup> The H<sub>2</sub>O<sub>2</sub> evolution from the two-electron oxygen reduction pathway needs the initial generation of the superoxide radical (O<sub>2</sub><sup>-</sup>) via a single-electron reduction (O<sub>2</sub> + e<sup>-</sup> → O<sub>2</sub><sup>-</sup>) process, followed by proton-coupled electron transfer to produce H<sub>2</sub>O<sub>2</sub> (O<sub>2</sub> + 2H<sup>+</sup> + e<sup>-</sup> → H<sub>2</sub>O<sub>2</sub>).<sup>9,10</sup> To improve the solar-to-H<sub>2</sub>O<sub>2</sub> efficiency, researchers have mainly focused on the rational design of suitable photocatalysts that are selective toward the two-electron oxygen reduction reaction (2e<sup>-</sup> ORR) and also suppress the competing side reactions: 2e<sup>-</sup> proton reduction to H<sub>2</sub> and 4e<sup>-</sup> ORR to H<sub>2</sub>O.<sup>11–14</sup>

Among the various photocatalysts investigated, graphitic carbon nitride (g-C<sub>3</sub>N<sub>4</sub> [CN]) has received tremendous research interest due to its unique features, such as suitable band gap for visible light absorption, proper valence, conduction band positions, and abundance of its constituents (i.e., N and C and high stability).<sup>15,16</sup> Most important, recent work demonstrates that CN-based photocatalysts exhibit activity for the 2e<sup>-</sup>-ORR pathway to selectively produce H<sub>2</sub>O<sub>2</sub> under visible light

### The bigger picture

Solar-driven two-electron oxygen reduction reaction (2e<sup>-</sup> ORR) provides a milder, safer, and lower carbon intensive approach for H<sub>2</sub>O<sub>2</sub> production compared with the industrial anthraquinone oxidation process. In this work, we screen carbon nitride-based photocatalysts via density functional theory (DFT) calculations by simultaneously taking H<sub>2</sub>O<sub>2</sub> generation and decomposition into consideration. The DFT results provide strong evidence and guidance to design a modified carbon nitride with heteroatomic oxygen at the pristine position of graphitic nitrogen and cyano groups coupled with amino nitrogen at the edge of crystalline nanosheets. The introduced heteroatomic oxygen efficiently reduces the overpotential for H<sub>2</sub>O<sub>2</sub> generation, while the cyano group plays a vital role in inhibiting the *in situ* H<sub>2</sub>O<sub>2</sub> decomposition. The screened photocatalyst is rationally synthesized, and unprecedented H<sub>2</sub>O<sub>2</sub> evolution is achieved via the 2e<sup>-</sup> ORR process along with ~100% acetone selectivity from isopropyl alcohol oxidation.

irradiation.<sup>12,17–19</sup> To improve the photocatalytic (PC) activity for H<sub>2</sub>O<sub>2</sub> production of bulk CN, various strategies have been developed to improve the utilization of photogenerated electrons and reduce the hydrogen evolution reaction such as nanostructure design,<sup>20,21</sup> heteroatoms doping,<sup>22,23</sup> defect engineering,<sup>24,25</sup> and the formation of heterojunctions with other semiconductors or metals.<sup>26,27</sup> However, the demonstrated yield of H<sub>2</sub>O<sub>2</sub> is usually in the scale of micromoles per hour and is distant from commercialization.<sup>6</sup> This is mainly due to the high overpotential (low limiting potential) for selective H<sub>2</sub>O<sub>2</sub> production in the 2e<sup>−</sup> ORR pathway.<sup>28</sup> However, designing a single active site to reduce overpotential is always accompanied by the rapid reverse reaction: H<sub>2</sub>O<sub>2</sub> decomposition.<sup>29</sup> In addition, limited visible-light absorption, low substrate (sacrificial agents) accessibility, and high charge carriers recombination are some of the key challenges for efficient CN-based PC H<sub>2</sub>O<sub>2</sub> production.<sup>30</sup>

The introduction of defects into the heptazine unit of CN is an effective strategy to modify its band-gap structure, extend light absorption, and improve charge separation capacity.<sup>31,32</sup> Among various point-defect engineering strategies, heteroatomic dopant (e.g., S and O) and cyano group introduction have demonstrated improved solar-driven H<sub>2</sub>O<sub>2</sub> production.<sup>33–35</sup> However, their roles in reducing overpotential for PC H<sub>2</sub>O<sub>2</sub> production and inhibiting H<sub>2</sub>O<sub>2</sub> decomposition are still lacking. In addition, the use of sacrificial agents (e.g., isopropyl alcohol) is always needed as electron donors to maintain PC H<sub>2</sub>O<sub>2</sub> production activity.<sup>36</sup> Using low-value sacrificial agents and/or selectively converting them valuable products is also crucial to drive its economically feasible toward PC H<sub>2</sub>O<sub>2</sub> production.

Here, we use density functional theory (DFT) calculations to systematically study the effects of heteroatomic oxygen doping and cyano group introduction (separately and simultaneously) on lowering the overpotential for H<sub>2</sub>O<sub>2</sub> formation and inhibiting H<sub>2</sub>O<sub>2</sub> decomposition over CN. The introduced heteroatomic oxygen in CN to partially replace pristine graphitic nitrogen is revealed to be the bifunctional active site for both H<sub>2</sub>O<sub>2</sub> production and decomposition, while the negatively charged cyano group synergistically reduces reaction overpotential for H<sub>2</sub>O<sub>2</sub> formation and provides a high potential barrier for H<sub>2</sub>O<sub>2</sub> decomposition. Following our DFT calculation, the target photocatalyst with fixed heteroatomic oxygen and cyano group is synthesized by a facile hydrothermal pretreatment and molten salt method. As a result, the as-fabricated photocatalyst exhibits record high H<sub>2</sub>O<sub>2</sub> production yield (5.57 mM/h) under visible light, along with selective acetone production (100% selectivity) from isopropanol oxidation. A reasonable amount of H<sub>2</sub>O<sub>2</sub> could also be produced in the presence of low-cost electron donors such as cellulosic biomass and its derivatives. Techno-economic analysis (TEA) is then conducted based on the demonstrated lab-scale performance to reveal the economic feasibility of PC H<sub>2</sub>O<sub>2</sub> production.

## RESULTS AND DISCUSSION

### Theoretical prediction of efficient photocatalyst

To understand the roles and functions of heteroatomic oxygen doping and cyano group introduction and guide the efficient catalyst design for PC H<sub>2</sub>O<sub>2</sub> production via 2e<sup>−</sup> ORR process, four types of model structures were established to represent pristine CN, oxygen doped CN (OCN), CN with cyano group (NCN), and CN with cyano group and heteroatomic oxygen (NOCN) with both edge- and basal-type active sites (Figure 1A). Various oxygen locations were included in the OCN and NOCN model structures to reveal the effect of oxygen functional groups such as O and OH (Figures S1 and S2). Figure 1B displays the calculated limiting potentials

<sup>1</sup>Department of Chemical and Petroleum Engineering, University of Calgary, 2500 University Drive, NW, Calgary, AB T2N 1N4, Canada

<sup>2</sup>Department of Chemistry, University of Calgary, 2500 University Drive, NW, Calgary, AB T2N 1N4, Canada

<sup>3</sup>Department of Geosciences, University of Calgary, 2500 University Drive, NW, Calgary, AB T2N 1N4, Canada

<sup>4</sup>These authors contributed equally

<sup>5</sup>Lead contact

\*Correspondence:  
[samira.siahrostami@ucalgary.ca](mailto:samira.siahrostami@ucalgary.ca) (S.S.),  
[md.kibria@ucalgary.ca](mailto:md.kibria@ucalgary.ca) (M.G.K.),  
[jinguang.hu@ucalgary.ca](mailto:jinguang.hu@ucalgary.ca) (J.H.)

<https://doi.org/10.1016/j.checat.2022.04.015>

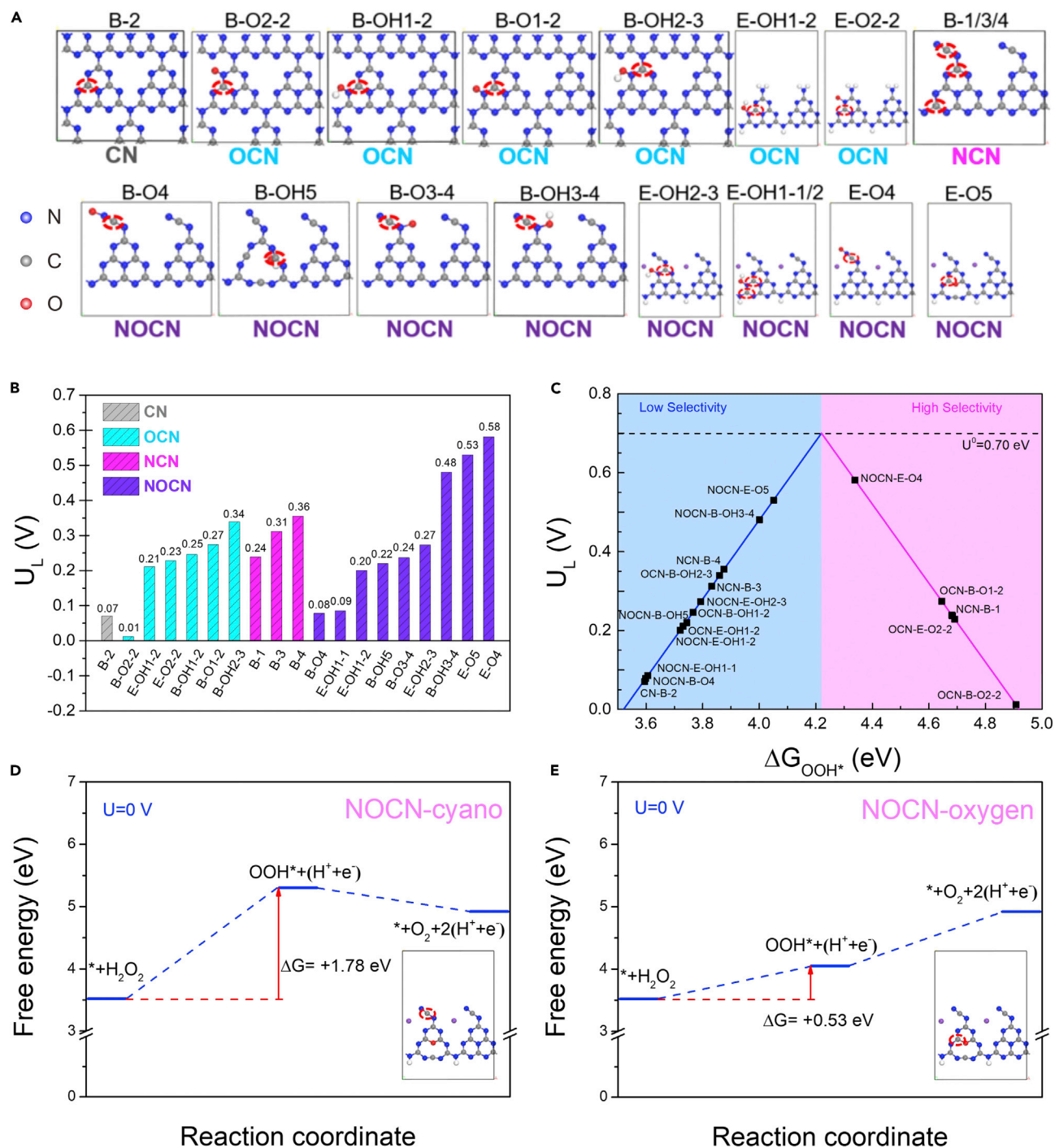


**Figure 1. DFT calculation of different model structures**

(A) Atomic structures representing different possible active sites in CN, OCN, NCN, and NOCN.

(B) Calculated limiting potentials for 2e<sup>-</sup> ORR over various model structures in (A).

(C) Activity volcano plots showing the calculated limiting potential as a function of  $\Delta G_{\text{OOH}^*}$ . Pink-shaded area represents the region with high selectivity toward the H<sub>2</sub>O<sub>2</sub> product.

(D) H<sub>2</sub>O<sub>2</sub> decomposition over the cyano group in NOCN.

(E) H<sub>2</sub>O<sub>2</sub> decomposition over heteroatomic oxygen in NOCN.

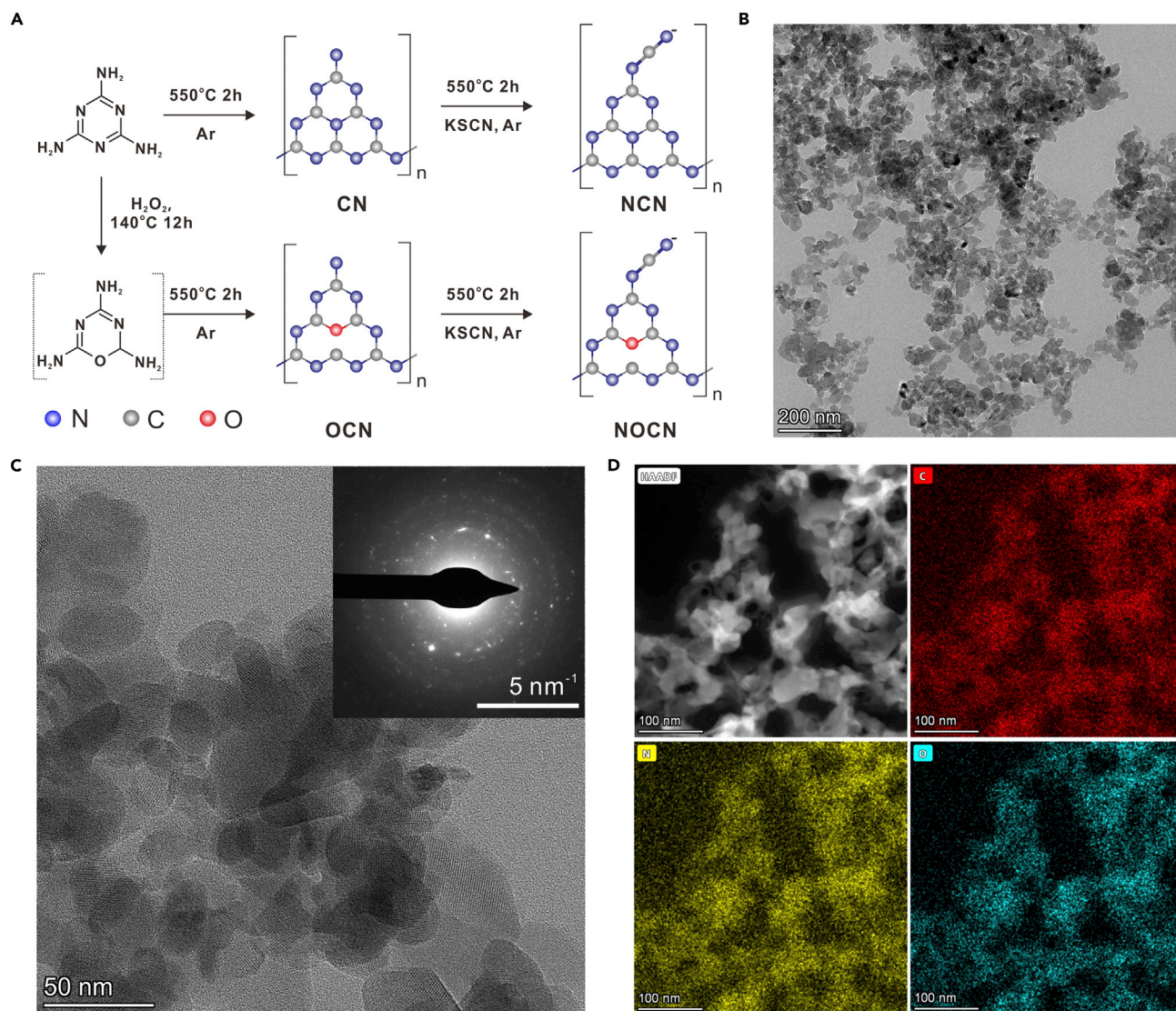
(the highest potential at which all of the elementary steps are downhill in free energy) for 2e<sup>-</sup> ORR on different active sites in CN, OCN, NCN, and NOCN. Higher limiting potential corresponds to lower overpotential, thus higher activity toward H<sub>2</sub>O<sub>2</sub> production. All of the edge- and basal-type models were screened for the limiting potential calculation (Figure S3). The limiting potential of CN is only 0.07 V, while the limiting potentials for most OCN are predicted to be 0.21–0.34 V. As an exception, the B-O2-2 shows even lower limiting potential (0.01 V), indicating the presence of heteroatomic oxygen, and its position is the key factor for enhancing H<sub>2</sub>O<sub>2</sub> production (Figure 1B). The introduction of NCN is revealed to have a similar contribution to H<sub>2</sub>O<sub>2</sub> production in regard to the calculated limiting potentials (0.24–0.36 V). Upon the introduction of oxygen and cyano groups simultaneously (NOCN structures), both calculated limiting potentials (0.08–0.58 V) and the number of active sites increase, which indicates their potential synergistic effect on boosting H<sub>2</sub>O<sub>2</sub> production.

Figure 1C displays the theoretical volcano plots using the limiting potential as a function of  $\Delta G_{\text{OOH}^*}$  for H<sub>2</sub>O<sub>2</sub> production. The pink-shaded area shows the region with high selectivity toward the H<sub>2</sub>O<sub>2</sub> product. This analysis shows how structural differences can influence the reactivity of CN, resulting in different H<sub>2</sub>O<sub>2</sub> production activity and selectivity. The NOCN-E-O4 has the highest 2e<sup>-</sup> ORR activity, with the maximum limiting potential of 0.58 V (Figure 1B). However, it also requires high formation energy (3.50 eV; Figure S4), resulting in an unstable structure. Thus, the most active site during the 2e<sup>-</sup> ORR should be the NOCN-E-O5, with a slightly lower limiting potential of 0.53 V, but much lower formation energy (0.76 eV; Figure S4). Meanwhile, the adsorption of O<sub>2</sub> on the models of CN, OCN, NCN, and NOCN was also systematically investigated (Figure S5). NOCN-E-O5 was further revealed to be the active site for H<sub>2</sub>O<sub>2</sub> generation as it has a properly strong O<sub>2</sub> adsorption, high limiting potential, and low formation energy.

The *in situ* decomposition of H<sub>2</sub>O<sub>2</sub> is another factor that limits the overall PC performance of the catalyst. Rational photocatalyst design should also take into consideration the H<sub>2</sub>O<sub>2</sub> decomposition inhibition. The *in situ* H<sub>2</sub>O<sub>2</sub> decomposition was then investigated on the active site of the cyano group and heteroatomic oxygen. The results clearly show that the H<sub>2</sub>O<sub>2</sub> decomposition is a typical endergonic reaction and the  $\Delta G$  from H<sub>2</sub>O<sub>2</sub> to OOH\* on the cyano group is 1.78 eV (Figure 1D), indicating that the introduced cyano group could efficiently inhibit the H<sub>2</sub>O<sub>2</sub> decomposition. On the one hand, although introduced oxygen contributes to H<sub>2</sub>O<sub>2</sub> generation by reducing the overpotential of O<sub>2</sub> activation, it also contributes to H<sub>2</sub>O<sub>2</sub> decomposition with the easy formation of OOH\* intermediates (Figure 1E). Here, the DFT calculations clearly show the oxygen doping acts as a bifunctional active site for accelerating H<sub>2</sub>O<sub>2</sub> production and decomposition. On the other hand, the introduced cyano group synergistically cooperates with doped oxygen to further reduce H<sub>2</sub>O<sub>2</sub> formation overpotential. More important, it also prevents *in situ* H<sub>2</sub>O<sub>2</sub> decomposition. The DFT results also unveil the best location for introducing oxygen (location of pristine graphitic nitrogen) and the cyano group in pristine CN for H<sub>2</sub>O<sub>2</sub> production.

### Catalyst design and characterization

According to the guidance from DFT calculations, photocatalysts with a specific molecular structure (NOCN-E-O5) should be precisely synthesized. Here, pristine CN was rationally modified to synthesize four different catalysts: doped with heteroatomic oxygen (OCN), doped with cyano group (NCN), and finally doped with oxygen and cyano group (NOCN). Briefly, CN was directly prepared by the calcination of



**Figure 2. Schematic illustration of the fabrication process and morphology of NOCN**

- (A) Schematic illustration of catalyst preparation.  
 (B) Transmission electron microscopy (TEM) image of NOCN.  
 (C) High-resolution TEM (HRTEM) image with selected area electron diffraction (SAED) pattern of NOCN.  
 (D) High-angle annular dark-field scanning TEM (HAADF-STEM) and corresponding elemental distributions.

melamine, while the calcination of pre-treated melamine with H<sub>2</sub>O<sub>2</sub> was used to partially replace pristine graphitic nitrogen according to the literature.<sup>37</sup> The Fourier transform infrared (FTIR) results confirmed the introduction of oxygen in melamine after hydrothermal treatment (Figure S6). The obtained CN and OCN were further functionalized by potassium thiocyanide (KSCN) to prepare NCN and NOCN with cyanamide defects, respectively (Figure 2A). The as-prepared CN exhibited bulk morphology, while the OCN from the pre-treated melamine showed the morphology of particles (Figure S7). Reduced sizes were achieved for the functionalized NCN and NOCN by KSCN. The NOCN is constructed by numerous exfoliated nanosheets with high crystallinity (Figures 2B and 2C), and the introduced oxygen dopant is also evenly distributed in the framework of NOCN (Figure 2D). The intercalation of K<sup>+</sup> could be revealed by the disappearance of in-plane packed heptazine

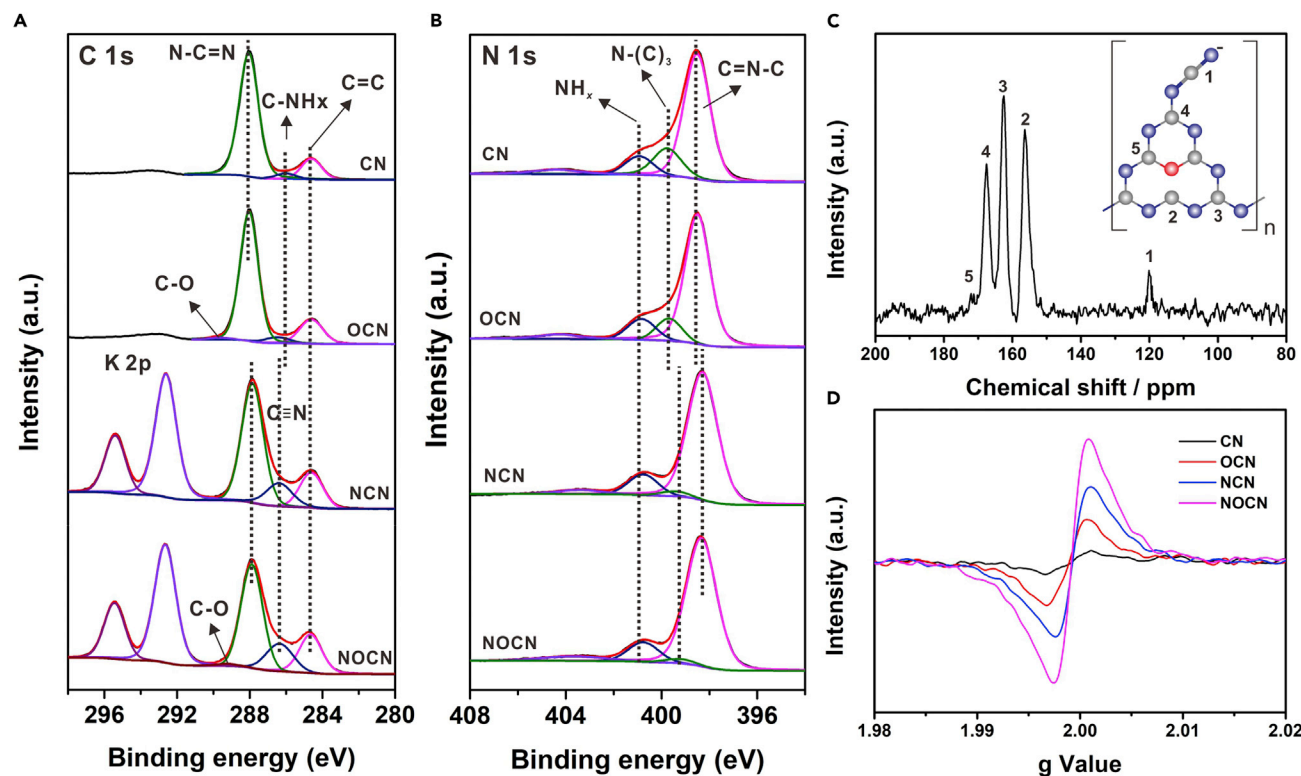


**Figure 3. Structural analysis of samples**

(A) C 1s high-resolution XPS spectra of CN, OCN, NCN, and NOCN.

(B) N 1s high-resolution XPS spectra of CN, OCN, NCN, and NOCN.

(C) Solid-state <sup>13</sup>C NMR spectrum of NOCN.

(D) ESR spectra of CN, OCN, NCN, and NOCN.

units (100) at approximately 13°, the shift of  $\pi$ - $\pi$  interlayer stacking (002) at approximately 27.4°, and the presence of peaks below 10° (Figure S8).<sup>25,38</sup> The characteristic infrared vibration of the N-H bond at 3,315 cm<sup>-1</sup> and 3,090 cm<sup>-1</sup> disappeared, and peaks at 2,122 cm<sup>-1</sup>, 2,080 cm<sup>-1</sup>, and 1,576 cm<sup>-1</sup> appeared in NCN and NOCN, indicating the introduction of the cyano group (C≡N) at the edges to replace the initial -NH<sub>2</sub> group (Figure S9).<sup>9</sup>

### Structural analysis of NOCN

The changes in chemical structure were further investigated by X-ray photoelectron spectroscopy (XPS). All of the XPS results were calibrated by the sp<sup>2</sup> C=C at 284.8 eV. It is clear that OCN and NOCN showed a typical O 1s peak, while NCN and NOCN showed typical K 2s, K 2p, and S 2p peaks (Figure S10), which is greatly consistent with a previous report.<sup>34</sup> The detected C-NH<sub>x</sub> in CN and OCN disappeared after functionalization by KSCN, indicating the replacement by the cyano group (C≡N) in NCN and NOCN (Figure 3A). The presence of doped oxygen with the formation of a C-O chemical bond was also confirmed in OCN and NOCN. The typical N-(C)<sub>3</sub> was detected in CN and OCN, while NCN and NOCN exhibited greatly reduced intensity and a significant shift to lower binding energy, indicating the introduction of nitrogen vacancy after functionalization by KSCN (Figure 3B). The carbon:nitrogen ratio was calculated to be 0.80, which is higher than the theoretical value of pristine CN (0.75), indicating the presence of nitrogen vacancy in NOCN. The oxygen content in NOCN was also calculated accordingly, and the value was 5.6%. Solid-state <sup>13</sup>C NMR demonstrated five types of carbon in the as-prepared NOCN, and the final

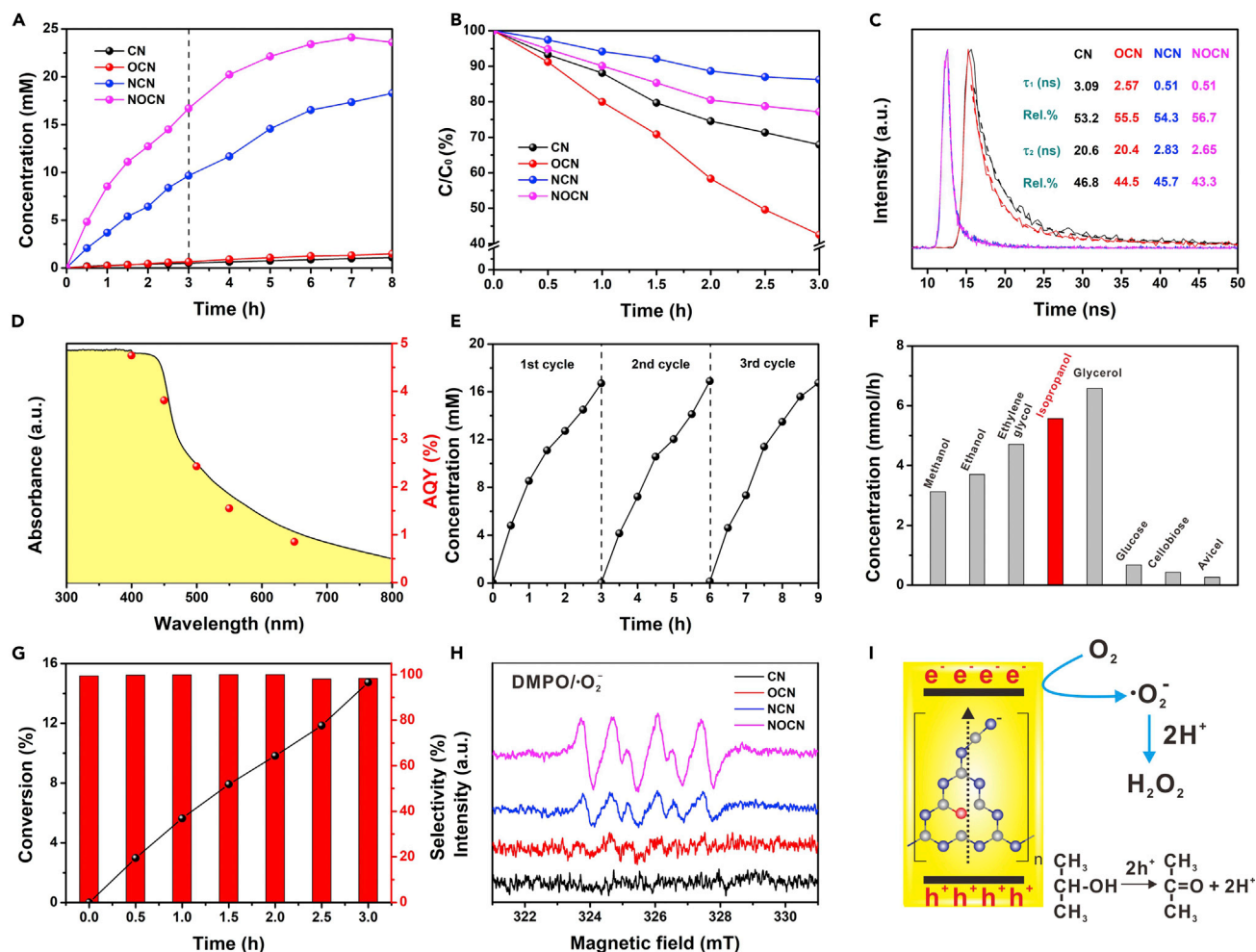


**Figure 4. Photocatalytic H<sub>2</sub>O<sub>2</sub> production of as-prepared samples**

- (A) Time course of H<sub>2</sub>O<sub>2</sub> production for different photocatalysts.  
 (B) H<sub>2</sub>O<sub>2</sub> decomposition over different photocatalysts.  
 (C) TRPL spectra with characteristic lifetime.  
 (D) UV-vis absorption spectrum and apparent quantum yield (AQY) of NOCN.  
 (E) Cycling test for photocatalytic H<sub>2</sub>O<sub>2</sub> production over NOCN.  
 (F) Photocatalytic H<sub>2</sub>O<sub>2</sub> production over NOCN in the presence of different electron donors.  
 (G) Isopropanol conversion and acetone selectivity during the photocatalytic H<sub>2</sub>O<sub>2</sub> production over NOCN.  
 (H) ESR signals of DMPO-O<sub>2</sub><sup>-</sup> over different photocatalysts.  
 (I) Proposed mechanism for photocatalytic H<sub>2</sub>O<sub>2</sub> production over NOCN.

atomic configuration of NOCN was illustrated based on the above characterization results (Figure 3C), which matches well with the DFT-calculated most active site (NOCN-E-O5) for the 2e<sup>-</sup> ORR process (Figure 1). The introduced oxygen and nitrogen vacancy both increased the content of structural defects (Figure 3D), which help to enhance light absorption and charge separation efficiency (Figure S11).<sup>33,39</sup>

### PC evaluation of catalysts

PC H<sub>2</sub>O<sub>2</sub> production was first evaluated over different photocatalysts in the presence of isopropanol as an electron donor. The presence of O<sub>2</sub> in the aqueous solution was revealed to be one of the essential factors for H<sub>2</sub>O<sub>2</sub> production (Figure S12). All of the photocatalysts exhibited an almost linear H<sub>2</sub>O<sub>2</sub> evolution rate during the first 3 h and then slowly plateaued (Figures 4A and S13). The pristine CN exhibited an

H<sub>2</sub>O<sub>2</sub> production rate of 0.17 mM/h within 3 h, while the OCN showed a slight increase to 0.22 mM/h. Although the introduced heteroatomic oxygen was proved to be the active site for H<sub>2</sub>O<sub>2</sub> production, as it can reduce the overpotential (Figure 1B), the preferred *in situ* H<sub>2</sub>O<sub>2</sub> decomposition leads to the limited overall H<sub>2</sub>O<sub>2</sub> generation activity (Figure 4B). The functionalized photocatalysts NCN and NOCN showed 3.22 and 5.57 mM/h H<sub>2</sub>O<sub>2</sub> evolution rates, respectively; these are 18.9 and 32.8 times higher than that of pristine CN, indicating the great synergistic effect of introduced oxygen and the cyano group. The H<sub>2</sub>O<sub>2</sub> production efficiency is consistent with the photoelectrochemical performance of these photocatalysts (Figure S14). The achieved H<sub>2</sub>O<sub>2</sub> production in this work has significantly improved compared to reports in the literature (Figure S15). The introduction of the cyano group was revealed to inhibit H<sub>2</sub>O<sub>2</sub> decomposition (Figure 4B), which is consistent with our DFT calculation (Figure 1D). The time-resolved transient photoluminescence (TRPL) spectra demonstrates the consistent trend of photoluminescence lifetimes with H<sub>2</sub>O<sub>2</sub> production activity over different photocatalysts (Figure 4C). The solar-to-H<sub>2</sub>O<sub>2</sub> production efficiency was evaluated by apparent quantum yield (AQY) under different monochromatic light conditions (Figure S16). The NOCN exhibited the highest AQY, 4.75%, and the trend is consistent with the light absorption spectrum (Figure 4D). The cycling test by recovering the photocatalyst after reaction demonstrated the outstanding recyclability and physicochemical stability of the NOCN photocatalyst (Figure 4E).

The H<sub>2</sub>O<sub>2</sub> production involves the photogenerated hole consumption with electron donor (sacrificial agent) and O<sub>2</sub> reduction by the photogenerated electrons.<sup>40</sup> Selecting a suitable electron donor (e.g., sustainable, efficient, low cost) and selectively converting it to a high-value product is an essential factor (but less explored) for the economically feasible PC H<sub>2</sub>O<sub>2</sub> generation. We investigated the efficiency of conventional alcohol electron donors (from C1 to C3) with different amounts of hydroxyl groups. We noticed that long-chain alcohol benefited H<sub>2</sub>O<sub>2</sub> production, and multiple hydroxyl groups also contributed to higher H<sub>2</sub>O<sub>2</sub> evolution activity (Figure 4F). In addition, we observed that biomass-derived components such as glucose, cellobiose, and avicel (crystalline cellulose) can also serve as electron donors for H<sub>2</sub>O<sub>2</sub> production, but at lower efficiency due to their more complex molecular structure. More important, the well-designed NOCN also exhibited considerable activity to produce H<sub>2</sub>O<sub>2</sub> in pure water (36.5 μM/h), without any sacrificial agents, which is lower than the activity in the presence of avicel as an electron donor (Figure S17). Since the selective conversion of the electron donor to valuable products is also equally important, we next explored the product profile of these small molecular electron donors (within three carbons) after photocatalysis. The results indicated that our rational designed photocatalyst (NOCN) could selectively convert isopropanol, the widely used sacrificial agent to timely consume photogenerated holes for H<sub>2</sub>O<sub>2</sub> production,<sup>41,42</sup> to acetone with 100% selectivity (Figure 4G). While other electron donors tested here showed more diverse products profiles. Electron spin resonance (ESR) was performed to confirm the mechanism for H<sub>2</sub>O<sub>2</sub> production. O<sub>2</sub><sup>-</sup> was revealed to be produced during the reaction, and the relative ESR intensity order was consistent with the H<sub>2</sub>O<sub>2</sub> production activity of different photocatalysts (Figure 4H). Here, based on our results and the previous literature,<sup>9,38</sup> the mechanism for H<sub>2</sub>O<sub>2</sub> production over NOCN was proposed (Figure 4I). The separated photogenerated electrons trigger the ORR to first produce O<sub>2</sub><sup>-</sup> and then two protons combine with O<sub>2</sub><sup>-</sup> to produce H<sub>2</sub>O<sub>2</sub>. Meanwhile, the photogenerated holes induce the isopropanol oxidation to selectively produce acetone. The introduced heteroatomic oxygen and cyano group synergistically reduces the overpotential for H<sub>2</sub>O<sub>2</sub> production, while the negatively charged cyano group inhibits the *in situ* decomposition of H<sub>2</sub>O<sub>2</sub>.

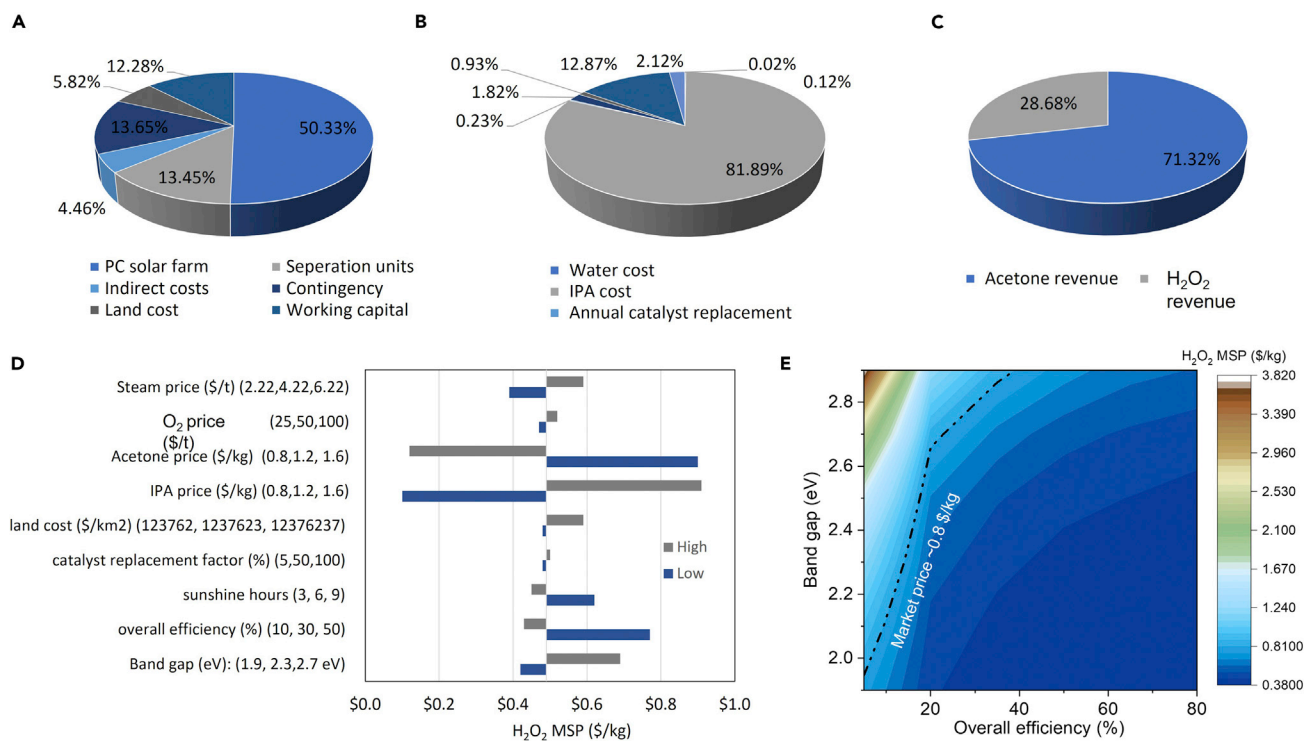


**Figure 5. Techno-economic analysis of photocatalytic H<sub>2</sub>O<sub>2</sub> production**

(A) CAPEX of photocatalytic H<sub>2</sub>O<sub>2</sub> production along with isopropanol oxidation.

(B) Annual OPEX of photocatalytic H<sub>2</sub>O<sub>2</sub> production along with isopropanol oxidation.

(C) Annual revenue of photocatalytic H<sub>2</sub>O<sub>2</sub> production along with isopropanol oxidation.

(D) Sensitivity analysis to illustrate the impact of changes in key parameters for the photocatalytic process.

(E) Contour plots of band gap (eV) versus overall efficiency (%). Black dashed line indicates the current (as of this writing) market price of H<sub>2</sub>O<sub>2</sub> (50%) at 0.8 US\$/kg.

### Techno-economic analysis

We carried out TEA of a potential PC system to produce H<sub>2</sub>O<sub>2</sub> via 2e<sup>-</sup> ORR, with isopropanol as electron donor. The objective of the TEA was to gauge catalyst performance and other cost targets needed to drive the economic feasibility of the process. The details of the plant design, methodology, and parameters used are described in the [experimental procedures](#). The capital expenditure (CAPEX) costs are dominated by the cost of the PC solar farm that is the individual reactors followed by the cost of the distillation columns (Figure 5A). The annual operating expenditure (OPEX) indicates that the isopropyl alcohol (IPA) cost is the major contributor followed by steam costs for the separation process (Figure 5B). This is understandable, as the envisioned solar-driven PC process would be a capital-intensive process with no energy costs associated with it, leading to the IPA cost playing a dominant role in the annual OPEX. Lastly, the produced H<sub>2</sub>O<sub>2</sub> contributes ~29% of the annual revenue, while acetone contributes ~71% to the annual revenue (Figure 5C). Compared with the mineralization of the sacrificial agents, the selective acetone production (~1.2 US\$/kg with ~85 t production per day) from IPA versus 50 t of H<sub>2</sub>O<sub>2</sub> production per day realizes the feasibility of this PC process.

Sensitivity analysis indicates that the minimum selling price (MSP) of H<sub>2</sub>O<sub>2</sub> is ~0.5 US\$/kg, which is lower than the current market price (MP) of ~0.8 US\$/kg for a high concentration (50%) of H<sub>2</sub>O<sub>2</sub> (Figure 5D). Among all of the parameters, IPA

and acetone prices play the biggest role in controlling the MSP of H<sub>2</sub>O<sub>2</sub>, while the cost of land and catalyst replacement are a negligible proportion (Table S1). Among the catalyst-related parameters, the band gap of catalyst and overall efficiency play a major role in driving economic feasibility. In a base scenario in which we have taken the catalyst band gap to be 2.3 eV and overall efficiency of 30%, the MSP of H<sub>2</sub>O<sub>2</sub> falls below the market price. This can be overcome by using low band-gap catalysts as depicted by the contour plot, revealing the interplay between these two critical parameters of band gap and efficiency (Figure 5E). A low band-gap material requires low overall efficiency, which limits the stability of the system. The use of a higher band gap and more stable photocatalysts increases the requirement of overall efficiency of the process. The results suggest that for our process, which selectively makes H<sub>2</sub>O<sub>2</sub> along with the valuable by-product acetone, low overall efficiencies of 10% are acceptable if a low band-gap (~2–2.1 eV) material is used that absorbs major fractions of sunlight.

### Conclusions

DFT calculations provide clear guidance for the modification of CN to boost PC H<sub>2</sub>O<sub>2</sub> generation. Heteroatomic oxygen and the cyano group are rationally introduced to synergistically reduce the overpotential for H<sub>2</sub>O<sub>2</sub> formation. Meanwhile, the negatively charged cyano group contributes to inhibiting the *in situ* decomposition of H<sub>2</sub>O<sub>2</sub>. As a result, 5.57 mM/h of H<sub>2</sub>O<sub>2</sub> generation is achieved on the NOCN photocatalyst with 100% acetone selectivity from isopropanol oxidation. Techno-economic analysis reveals the target overall efficiency and band gap to make our proposed process economically compelling for practical applications. This current work sheds light on designing photocatalysts for boosting H<sub>2</sub>O<sub>2</sub> production in solar energy conversion.

## EXPERIMENTAL PROCEDURES

### Resource availability

#### Lead contact

Further information and requests for resources should be directed to and will be fulfilled by the lead contact, Jinguang Hu ([jinguang.hu@ucalgary.ca](mailto:jinguang.hu@ucalgary.ca)).

#### Materials availability

Full experimental and spectroscopy measurement details can be found in the [supplemental information](#).

#### Data and code availability

All of the data supporting this study are available in the manuscript and [supplemental information](#).

### Photocatalyst synthesis

All of the chemicals were purchased from Millipore Sigma and were not purified further. Typically, 7.2 g melamine was added into the solution of 15 mL H<sub>2</sub>O<sub>2</sub> and 35 mL deionized (DI) water with sonication for 10 min. The suspension was sealed in a 75-mL Teflon-lined autoclave and heated to 140°C for 12 h. The obtained white solid (oxygen-doped melamine) was washed with DI water and ethanol 3 times and dried in an oven overnight at 60°C. Oxygen-doped melamine was then annealed at 550°C for 2 h with a ramp rate of 0.5°C/min in argon to prepare yellow OCN. The obtained OCN (0.5 g) was mixed with 1 g KSCN, and the mixture was fully grounded before calcination at 550°C for 4 h with a ramp rate of 5°C/min in argon to prepare OCN with cyanamide defects (NOCN). Pristine CN and CN with cyanamide defects (NCN) were also synthesized accordingly.

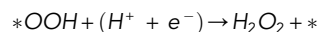
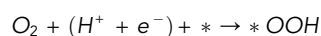
### PC H<sub>2</sub>O<sub>2</sub> production

A PC H<sub>2</sub>O<sub>2</sub> test was performed on a commercial PQ256 off-line reactor from Beijing Perfectlight (Figure S18). Typically, 50 mg photocatalyst was dispersed in a 100-mL 10 vol % isopropanol solution with sonication for 0.5 h. The system was purged with oxygen during the whole reaction. A 300-W Xenon lamp (Excelitas Technologies) was used as the light source. A 1.5-mL solution was sampled every 0.5 h and centrifuged to remove photocatalyst. A 1-mL supernatant was mixed with a 1-mL 0.1 mol/L potassium hydrogen phthalate aqueous solution and a 1-mL 0.4 mol/L potassium iodide (KI) aqueous solution. The above solution was kept for 1 h and the H<sub>2</sub>O<sub>2</sub> concentration was determined by UV-visible light (vis) spectroscopy at 350 nm, which is ascribed to the light absorbance of triiodide anions (I<sub>3</sub><sup>-</sup>) from the reaction H<sub>2</sub>O<sub>2</sub> + 3I<sup>-</sup> + 2H<sup>+</sup> → I<sub>3</sub><sup>-</sup> + 2H<sub>2</sub>O. The liquid products from electron donors were analyzed by high-performance liquid chromatography (HPLC, 1200 Agilent system) equipped with a refractive index detector (RID). The column was Hi-Plex H (6.5 × 300 mm, 8 μm, Agilent) and 0.005 M H<sub>2</sub>SO<sub>4</sub> was used as an eluting solvent with a flow rate of 0.6 mL/min.

### Computational details

We used DFT calculations with Vienna *ab initio* Simulation Package (VASP) code.<sup>43</sup> The projector augmented wave (PAW) method was used to describe the interactions between the electrons and ion cores.<sup>44</sup> The electron exchange and correlation energy were described using the Bayesian error estimation functional with van der Waals correlation (BEEF-vdW) function.<sup>45</sup> A plane-wave cutoff energy of 500 eV was used to expand the wave functions. The total energy convergence was set to be lower than 10<sup>-6</sup> eV, and the convergence criterion for geometry optimizations was a maximum force of 0.02 eV/Å. Four types of periodic CN monolayers were constructed to describe CN, OCN, NCN, and NOCN, as shown in Figure 4A. The Monkhorst-Pack method was used for k-point sampling, and more than 12 Å of vacuum in the z direction was adopted to separate the slabs.

The two-electron reaction pathway for ORR can be written as:



The reaction-free energy of each elementary step for the ORR is calculated using the computational hydrogen electrode model developed by Nørskov et al.<sup>46</sup> Frequency corrections were added to the calculated electronic energies as follows:

$$\Delta G = \Delta E + \Delta ZPE - T\Delta S + \Delta G_U + \Delta G_{pH} + \Delta G_{field}$$

$$\Delta G_U = eU$$

$$\Delta G_{pH} = 0.0592 \times pH,$$

where  $\Delta E$  is the total energy change obtained from DFT calculations,  $\Delta ZPE$  is the change of zero-point energy,  $T$  is the temperature (298.15 K), and  $\Delta S$  represents the change of entropy.  $U$  is the electrode potential (versus reversible hydrogen electrode), and  $e^-$  is the charge transferred.  $\Delta G_{field}$  is the free energy correction due to the electrochemical double layer and is neglected as in previous studies.<sup>46,47</sup> Zero-point energy and entropies of the adsorbed species were calculated from the vibrational frequencies. Under  $pH = 0$  and  $U = 0$  V,  $G(H^+ + e^-) = \frac{1}{2}G(H_2)$ . The free energies of H<sub>2</sub>O and O<sub>2</sub> were calculated from gas-phase H<sub>2</sub>O at 0.035 bar, H<sub>2</sub> at 1 bar, 298.15 K, and  $2G(H_2O) - 2G(H_2) - G(O_2) = -4.92$  eV.

In addition, we studied the stabilities of the OCN and NOCN structure by calculating their formation energies as follows:

$$\Delta E_d(O) = E_O - E_d - n_O \mu_O,$$

where  $E_O$  and  $E_d$  are the total energies of OCN and NOCN structures with and without oxygen introduction, and  $n_O$  and  $\mu_O$  are the number and the chemical potential of oxygen, respectively.

### TEA

The TEA analysis was conducted for a plant designed to produce 50,000 kg<sub>H<sub>2</sub>O<sub>2</sub></sub>/day, operate for 350 days/year, with a plant lifetime of 20 years, and a depreciation lifetime of 10 years. The plant was designed based on a production and separation plant (Figure S19A). The PC production plant consists of multiple individual PC modules replicating the design of solar photovoltaic (PV) plants. Figure S19B is a block flow diagram of the methodology adopted to calculate the rate of production, the respective plant size/area needed, and the associated costs. The base case assumptions of process parameters are listed in Table S2.

The individual PC modules were designed to be 1 m<sup>2</sup> sized UV-transparent polymethyl methacrylate (PMMA) boxes inside which catalyst-coated PMMA sheets are placed. The catalyst thickness was assumed to be 50 μm and the density of the film was assumed to be the same as bulk CN at 2.336 g/cm<sup>3</sup>. A detailed schematic showing the design features of the individual PC module is presented in Figure S20. A 1.3-M isopropanol solution along with O<sub>2</sub> is fed into the PC modules through a series of pumps in which, under sunlight, irradiation photocatalyst material selectively generates H<sub>2</sub>O<sub>2</sub>, with acetone as the valuable by-product.

The material balance was calculated based on Equations 1 and 2:

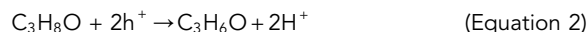


Figure S21 shows the sunlight irradiance at sea level, which was used in combination with the band gap of the catalyst to calculate the available photon flux for the photocatalyst material. The liquid separation process, which consisted of two distillation columns, was modeled using Aspen Plus version 10.0, and capital and utility costs were estimated using the Aspen Process Economic Analyzer version 10.0. High-concentration H<sub>2</sub>O<sub>2</sub> was produced at the outlet of the distillation columns at ~50% concentration (the remainder is water), while the acetone purity was ~98%. The financial parameters used are summarized in Table S3 and the cost parameters are summarized in Table S4.

### SUPPLEMENTAL INFORMATION

Supplemental information can be found online at <https://doi.org/10.1016/j.checat.2022.04.015>.

### ACKNOWLEDGMENTS

This work is financially supported by the Canada First Research Excellence Fund (CFREF).

### AUTHOR CONTRIBUTIONS

Methodology, H.Z. Investigation, H.Z. Writing – original draft, H.Z. Writing – review & editing, H.Z., S.L., S.S., M.G.K., and J.H. Investigation – DFT calculation, Q.J. and

S.S. Techno-economic analysis, M.A.K. Supervision, M.G.K. and J.H. Validation, M.G.K. and J.H. Funding acquisition, J.H. All of the authors discussed the results and reviewed this manuscript.

## DECLARATION OF INTERESTS

The authors declare no competing interests.

Received: March 9, 2022

Revised: April 13, 2022

Accepted: April 22, 2022

Published: May 12, 2022

## REFERENCES

- Sun, Y.Y., Han, L., and Strasser, P. (2020). A comparative perspective of electrochemical and photochemical approaches for catalytic H<sub>2</sub>O<sub>2</sub> production. *Chem. Soc. Rev.* 49, 6605–6631. <https://doi.org/10.1039/d0cs00458h>.
- Kim, H.W., Ross, M.B., Kornienko, N., Zhang, L., Guo, J.H., Yang, P.D., and McCloskey, B.D. (2018). Efficient hydrogen peroxide generation using reduced graphene oxide-based oxygen reduction electrocatalysts. *Nat. Catal.* 1, 282–290. <https://doi.org/10.1038/s41929-018-0044-2>.
- Xia, C., Back, S., Ringe, S., Jiang, K., Chen, F.H., Sun, X.M., Siahrostami, S., Chan, K.R., and Wang, H.T. (2020). Confined local oxygen gas promotes electrochemical water oxidation to hydrogen peroxide. *Nat. Catal.* 3, 125–134. <https://doi.org/10.1038/s41929-019-0402-8>.
- Campos-Martin, J.M., Blanco-Brieva, G., and Fierro, J.L.G. (2006). Hydrogen peroxide synthesis: an outlook beyond the anthraquinone process. *Angew. Chem. Int. Ed.* 45, 6962–6984. <https://doi.org/10.1002/anie.200503779>.
- Hou, H.L., Zeng, X.K., and Zhang, X.W. (2020). Production of hydrogen peroxide by photocatalytic processes. *Angew. Chem. Int. Ed.* 59, 17356–17376. <https://doi.org/10.1002/anie.201911609>.
- Zeng, X.K., Liu, Y., Hu, X.Y., and Zhang, X.W. (2021). Photoredox catalysis over semiconductors for light-driven hydrogen peroxide production. *Green. Chem.* 23, 1466–1494. <https://doi.org/10.1039/d0gc04236f>.
- Liu, J.L., Zou, Y.S., Jin, B.J., Zhang, K., Kan, Z., and Park, J.H. (2019). Hydrogen peroxide production from solar Water oxidation. *ACS Energy Lett.* 4, 3018–3027. <https://doi.org/10.1021/acsenergylett.9b02199>.
- Liu, Y., Wang, H., Yuan, X., Wu, Y., Wang, H., Tan, Y.Z., and Chew, J.W. (2021). Roles of sulfur-edge sites, metal-edge sites, terrace sites, and defects in metal sulfides for photocatalysis. *Chem. Catal.* 1, 44–68. <https://doi.org/10.1016/j.cheecat.2021.01.002>.
- Feng, C., Tang, L., Deng, Y., Wang, J., Luo, J., Liu, Y., Ouyang, X., Yang, H., Yu, J., and Wang, J. (2020). Synthesis of leaf-vein-like g-C<sub>3</sub>N<sub>4</sub> with tunable band structures and charge transfer properties for selective photocatalytic H<sub>2</sub>O<sub>2</sub> evolution. *Adv. Funct. Mater.* 30, 2001922. <https://doi.org/10.1002/adfm.202001922>.
- Wei, Z., Liu, M.L., Zhang, Z.J., Yao, W.Q., Tan, H.W., and Zhu, Y.F. (2018). Efficient visible-light-driven selective oxygen reduction to hydrogen peroxide by oxygen-enriched graphitic carbon nitride polymers. *Energy Environ. Sci.* 11, 2581–2589. <https://doi.org/10.1039/c8ee01316k>.
- Liu, Y., Zhao, Y.J., Sun, Y., Cao, J.J., Wang, H., Wang, X., Huang, H., Shao, M.W., Liu, Y., and Kang, Z.H. (2020). A 4e<sup>-</sup>-2e<sup>-</sup> cascaded pathway for highly efficient production of H<sub>2</sub> and H<sub>2</sub>O<sub>2</sub> from water photo-splitting at normal pressure. *Appl. Catal. B Environ.* 270, 118875. <https://doi.org/10.1016/j.apcatb.2020.118875>.
- Teng, Z.Y., Zhang, Q.T., Yang, H.B., Kato, K., Yang, W.J., Lu, Y.R., Liu, S.X., Wang, C.Y., Yamakata, A., Su, C.L., et al. (2021). Atomically dispersed antimony on carbon nitride for the artificial photosynthesis of hydrogen peroxide. *Nat. Catal.* 4, 374–384. <https://doi.org/10.1038/s41929-021-00605-1>.
- Xue, Z.H., Luan, D.Y., Zhang, H.B., (David) Lou, X.W., and Lou, X.W. (2022). Single-atom catalysts for photocatalytic energy conversion. *Joule* 6, 92–133. <https://doi.org/10.1016/j.joule.2021.12.011>.
- Wu, X., Zhang, H.B., Zuo, S.W., Dong, J.C., Li, Y., Zhang, J., and Han, Y. (2021). Engineering the coordination sphere of isolated active sites to explore the intrinsic activity in single-atom catalysts. *Nano-micro Lett.* 13, 136. <https://doi.org/10.1007/s40820-021-00668-6>.
- Ong, W.J., Tan, L.L., Ng, Y.H., Yong, S.T., and Chai, S.P. (2016). Graphitic carbon nitride (g-C<sub>3</sub>N<sub>4</sub>)-based photocatalysts for artificial photosynthesis and environmental remediation: are we a step closer to achieving sustainability? *Chem. Rev.* 116, 7159–7329. <https://doi.org/10.1021/acs.chemrev.6b00075>.
- Xu, G.L., Zhang, H.B., Wei, J., Zhang, H.X., Wu, X., Li, Y., Li, C.S., Zhang, J., and Ye, J.H. (2018). Integrating the g-C<sub>3</sub>N<sub>4</sub> nanosheet with B-H bonding decorated metal-organic framework for CO<sub>2</sub> activation and photoreduction. *ACS Nano* 12, 5333–5340. <https://doi.org/10.1021/acsnano.8b00110>.
- Wu, S., Yu, H.T., Chen, S., and Quan, X. (2020). Enhanced Photocatalytic H<sub>2</sub>O<sub>2</sub> production over carbon nitride by doping and defect engineering. *ACS Catal.* 10, 14380–14389. <https://doi.org/10.1021/acscatal.0c03359>.
- Moon, G.H., Fujitsuka, M., Kim, S., Majima, T., Wang, X.C., and Choi, W. (2017). Eco-friendly photochemical production of H<sub>2</sub>O<sub>2</sub> through O<sub>2</sub> reduction over carbon nitride frameworks incorporated with multiple heteroelements. *ACS Catal.* 7, 2886–2895. <https://doi.org/10.1021/acscatal.6b03334>.
- Shi, L., Yang, L.Q., Zhou, W., Liu, Y.Y., Yin, L.S., Hai, X., Song, H., and Ye, J.H. (2018). Photoassisted construction of holey defective g-C<sub>3</sub>N<sub>4</sub> photocatalysts for efficient visible-light-driven H<sub>2</sub>O<sub>2</sub> production. *Small* 14, 1703142. <https://doi.org/10.1002/sml.201703142>.
- Sun, J.H., Zhang, J.S., Zhang, M.W., Antonietti, M., Fu, X.Z., and Wang, X.C. (2012). Bioinspired hollow semiconductor nanospheres as photosynthetic nanoparticles. *Nat. Commun.* 3, 1139–1147. <https://doi.org/10.1038/ncomms2152>.
- Pan, Y., Liu, X.J., Zhang, W., Shao, B.B., Liu, Z.F., Liang, Q.H., Wu, T., He, Q.Y., Huang, J., Peng, Z., and Zhao, C. (2022). Bifunctional template-mediated synthesis of porous ordered g-C<sub>3</sub>N<sub>4</sub> decorated with potassium and cyano groups for effective photocatalytic H<sub>2</sub>O<sub>2</sub> evolution from dual-electron O<sub>2</sub> reduction. *Chem. Eng. J.* 427, 132032. <https://doi.org/10.1016/j.cej.2021.132032>.
- Guo, S.E., Deng, Z.P., Li, M.X., Jiang, B.J., Tian, C.G., Pan, Q.J., and Fu, H.G. (2016). Phosphorus-doped carbon nitride tubes with layered micro-nanostructure for enhanced visible-light photocatalytic hydrogen evolution. *Angew. Chem. Int. Ed.* 55, 1830–1834. <https://doi.org/10.1002/anie.201508505>.
- Chu, C.C., Miao, W., Li, Q.J., Wang, D.D., Liu, Y., and Mao, S. (2022). Highly efficient photocatalytic H<sub>2</sub>O<sub>2</sub> production with cyano and SnO<sub>2</sub> co-modified g-C<sub>3</sub>N<sub>4</sub>. *Chem. Eng. J.* 428, 132531. <https://doi.org/10.1016/j.cej.2021.132531>.
- Lau, V.W.H., Yu, V.W.Z., Ehrat, F., Botari, T., Moudrakovski, I., Simon, T., Duppel, V., Medina, E., Stolarczyk, J.K., Feldmann, J., et al. (2017). Urea-modified carbon nitrides: enhancing photocatalytic hydrogen evolution by rational defect engineering. *Adv. Energy Mater.* 7, 1602251. <https://doi.org/10.1002/aenm.201602251>.
- Lau, V.W.H., Moudrakovski, I., Botari, T., Weinberger, S., Mesch, M.B., Duppel, V., Senker, J., Blum, V., and Lotsch, B.V. (2016). Rational design of carbon nitride

- photocatalysts by identification of cyanamide defects as catalytically relevant sites. *Nat. Commun.* **7**, 12165–12210. <https://doi.org/10.1038/ncomms12165>.
26. Li, C.M., Du, Y.H., Wang, D.P., Yin, S.M., Tu, W.G., Chen, Z., Kraft, M., Chen, G., and Xu, R. (2017). Unique P-Co-N surface bonding states constructed on g-C<sub>3</sub>N<sub>4</sub> nanosheets for drastically enhanced photocatalytic activity of H<sub>2</sub> evolution. *Adv. Funct. Mater.* **27**, 1604328. <https://doi.org/10.1002/adfm.201604328>.
27. Wu, X.X., Zhao, H., Khan, M.A., Maity, P., Al-Attas, T., Larter, S., Yong, Q., Mohammed, O.F., Kibria, M.G., and Hu, J.G. (2020). Sunlight-driven biomass photorefinery for coproduction of sustainable hydrogen and value-added biochemicals. *ACS Sustain. Chem. Eng.* **8**, 15772–15781. <https://doi.org/10.1021/acssuschemeng.0c06282>.
28. Siahrostami, S., Li, G.L., Viswanathan, V., and Norskov, J.K. (2017). One- or two-electron water oxidation, hydroxyl radical, or H<sub>2</sub>O<sub>2</sub> evolution. *J. Phys. Chem. Lett.* **8**, 1157–1160. <https://doi.org/10.1021/acs.jpclett.6b02924>.
29. Chu, C.H., Zhu, Q.H., Pan, Z.H., Gupta, S., Huang, D.H., Du, Y.H., Weon, S., Wu, Y.A., Muhich, C., Stavitski, E., et al. (2020). Spatially separating redox centers on 2D carbon nitride with cobalt single atom for photocatalytic H<sub>2</sub>O<sub>2</sub> production. *P Natl. Acad. Sci. U S A* **117**, 6376–6382. <https://doi.org/10.1073/pnas.1913403117>.
30. Han, Q., Wang, B., Gao, J., Cheng, Z.H., Zhao, Y., Zhang, Z.P., and Qu, L.T. (2016). Atomically thin mesoporous nanomesh of graphitic C<sub>3</sub>N<sub>4</sub> for high-efficiency photocatalytic hydrogen evolution. *ACS Nano* **10**, 2745–2751. <https://doi.org/10.1021/acsnano.5b07831>.
31. Kumar, A., Raizada, P., Hosseini-Bandegharaei, A., Thakur, V.K., Nguyen, V.H., and Singh, P. (2021). C-N-Vacancy defect engineered polymeric carbon nitride towards photocatalysis: viewpoints and challenges. *J. Mater. Chem. A* **9**, 111–153. <https://doi.org/10.1039/d0ta08384d>.
32. Yu, H.J., Shi, R., Zhao, Y.X., Bian, T., Zhao, Y.F., Zhou, C., Waterhouse, G.I.N., Wu, L.Z., Tung, C.H., and Zhang, T.R. (2017). Alkali-assisted synthesis of nitrogen deficient graphitic carbon nitride with tunable band structures for efficient visible-light-driven hydrogen evolution. *Adv. Mater.* **29**, 1605148. <https://doi.org/10.1002/adma.201605148>.
33. Chen, L., Chen, C., Yang, Z., Li, S., Chu, C.H., and Chen, B.L. (2021). Simultaneously tuning band structure and oxygen reduction pathway toward high-efficient photocatalytic hydrogen peroxide production using cyano-rich graphitic carbon nitride. *Adv. Funct. Mater.* **31**, 2105731. <https://doi.org/10.1002/adfm.202105731>.
34. Zhang, P., Tong, Y.W., Liu, Y., Vequizo, J.J.M., Sun, H.W., Yang, C., Yamakata, A., Fan, F.T., Lin, W., Wang, X.C., and Choi, W. (2020). Heteroatom dopants promote two-electron O<sub>2</sub> reduction for photocatalytic production of H<sub>2</sub>O<sub>2</sub> on polymeric carbon nitride. *Angew. Chem. Int. Ed.* **59**, 16209–16217. <https://doi.org/10.1002/anie.202006747>.
35. Jourshabani, M., Asrami, M.R., and Lee, B.K. (2022). An efficient and unique route for the fabrication of highly condensed oxygen-doped carbon nitride for the photodegradation of synchronous pollutants and H<sub>2</sub>O<sub>2</sub> production under ambient conditions. *Appl. Catal. B Environ.* **302**, 120839. <https://doi.org/10.1016/j.apcatb.2021.120839>.
36. Volokh, M., and Shalom, M. (2021). Light on peroxide. *Nat. Catal.* **4**, 350–351. <https://doi.org/10.1038/s41929-021-00620-2>.
37. Sun, S.D., Li, J., Cui, J., Gou, X.F., Yang, Q., Liang, S.H., Yang, Z.M., and Zhang, J.M. (2018). Constructing oxygen-doped g-C<sub>3</sub>N<sub>4</sub> nanosheets with an enlarged conductive band edge for enhanced visible-light-driven hydrogen evolution. *Inorg. Chem. Front.* **5**, 1721–1727. <https://doi.org/10.1039/c8qi00242h>.
38. Zhang, J.Z., Yu, C.Y., Lang, J.Y., Zhou, Y.F., Zhou, B.X., Hu, Y.H., and Long, M.C. (2020). Modulation of Lewis acidic-basic sites for efficient photocatalytic H<sub>2</sub>O<sub>2</sub> production over potassium intercalated tri-s-triazine materials. *Appl. Catal. B Environ.* **277**, 119225. <https://doi.org/10.1016/j.apcatb.2020.119225>.
39. Wang, Y.X., Wang, H., Chen, F.Y., Cao, F., Zhao, X.H., Meng, S.G., and Cui, Y.J. (2017). Facile synthesis of oxygen doped carbon nitride hollow microsphere for photocatalysis. *Appl. Catal. B Environ.* **206**, 417–425. <https://doi.org/10.1016/j.apcatb.2017.01.041>.
40. Tsukamoto, D., Shiro, A., Shiraishi, Y., Sugano, Y., Ichikawa, S., Tanaka, S., and Hirai, T. (2012). Photocatalytic H<sub>2</sub>O<sub>2</sub> production from ethanol/O<sub>2</sub> system using TiO<sub>2</sub> loaded with Au-Ag bimetallic alloy nanoparticles. *ACS Catal.* **2**, 599–603. <https://doi.org/10.1021/cs2006873>.
41. Burek, B.O., Bahnemann, D.W., and Bloh, J.Z. (2019). Modeling and optimization of the photocatalytic reduction of molecular oxygen to hydrogen peroxide over titanium dioxide. *ACS Catal.* **9**, 25–37. <https://doi.org/10.1021/acscatal.8b03638>.
42. Wang, Y.B., Meng, D., and Zhao, X. (2020). Visible-light-driven H<sub>2</sub>O<sub>2</sub> production from O<sub>2</sub> reduction with nitrogen vacancy-rich and porous graphitic carbon nitride. *Appl. Catal. B Environ.* **273**, 119064. <https://doi.org/10.1016/j.apcatb.2020.119064>.
43. Kresse, G., and Furthmüller, J. (1996). Efficient iterative schemes for ab initio total-energy calculations using a plane-wave basis set. *Phys. Rev. B* **54**, 11169–11186. <https://doi.org/10.1103/physrevb.54.11169>.
44. Mortensen, J.J., Hansen, L.B., and Jacobsen, K.W. (2005). Real-space grid implementation of the projector augmented wave method. *Phys. Rev. B* **71**, 035109. <https://doi.org/10.1103/physrevb.71.035109>.
45. Wellendorff, J., Lundgaard, K.T., Mogelhoff, A., Petzold, V., Landis, D.D., Norskov, J.K., Bligaard, T., and Jacobsen, K.W. (2012). Density functionals for surface science: exchange-correlation model development with Bayesian error estimation. *Phys. Rev. B* **85**, 235149. <https://doi.org/10.1103/physrevb.85.235149>.
46. Norskov, J.K., Rossmeisl, J., Logadottir, A., Lindqvist, L., Kitchin, J.R., Bligaard, T., and Jonsson, H. (2004). Origin of the overpotential for oxygen reduction at a fuel-cell cathode. *J. Phys. Chem. B* **108**, 17886–17892. <https://doi.org/10.1021/jp047349j>.
47. Kattel, S., Atanassov, P., and Kiefer, B. (2012). Density functional theory study of Ni-N<sub>x</sub>/C electrocatalyst for oxygen reduction in alkaline and acidic media. *J. Phys. Chem. C* **116**, 17378–17383. <https://doi.org/10.1021/jp3044708>.